npj | digital medicine

Article

Published in partnership with Seoul National University Bundang Hospital

https://doi.org/10.1038/s41746-026-02792-2

Deep chemical structure graph learning deciphers the lipotoxicity code of hypertriglyceridemic pancreatitis

Check for updates

Anliang Huang[1,8], Qihang Yuan[1,8], Junhong Chen[2,8], Lei Wang[3,8], Yanlong Yu[4], Yunshu Zhang[1], Shurong Ma[1], Kai Liu[2], Zeming Wu[5], Shengji Cao[6] ✉, Tianyi Liu[7] ✉, Dong Shang[1] ✉ & Peiyuan Yin[1] ✉

The discrepancy between serum triglyceride levels and the clinical severity of hyperlipidemic acute pancreatitis (HLAP) complicates risk stratification. Traditional lipidomics, which primarily rely on linear abundance, often fail to distinguish the HLAP-specific lipidome from the metabolic background of hypertriglyceridemia (HTG). To overcome this limitation, DeepLipiDecipher was developed as a knowledge-guided graph neural network framework that integrates lipid chemical structures with metabolic topology to identify latent lipotoxic features. In a retrospective cohort of 433 subjects, DeepLipiDecipher demonstrated robust classification performance (AUC = 0.810), effectively distinguishing the HLAP phenotype and outperforming conventional machine learning models. Interpretability analysis revealed that HLAP susceptibility correlated with a distinct structural lipid profile, marked by the synergistic enrichment of polyunsaturated and ether-linked phospholipids, rather than total lipid mass. Moreover, computational causal inference implicated a pathogenic mechanism wherein SMPD3-mediated ceramide accumulation induced basal cytotoxicity, and PTGS2 hyperactivation promoted the peroxidation of these vulnerable lipids, triggering systemic inflammation. These results highlight the value of incorporating network topology into lipidomic analysis and suggest the network-inferred SMPD3-Ceramide-PTGS2 immunometabolic axis as a potential therapeutic target for preventing the progression from metabolic dysfunction to acute organ injury.

Acute pancreatitis (AP) is a common gastrointestinal emergency, with hypertriglyceridemia (HTG) emerging as a leading cause alongside cholelithiasis, driven by the global rise in metabolic syndrome[1,2]. Epidemiological data suggest that serum triglyceride (TG) levels exceeding 20 mmol/L increase the risk of AP by thirteen-fold compared to normolipidemic baselines[3]. However, the relationship between lipid levels and clinical severity remains notably non-linear. Some patients with severe HTG remain asymptomatic, while others with moderate lipid elevation develop fulminant pancreatitis. This discrepancy, often referred to as the HTG paradox, highlights the limitations of relying solely on biochemical markers for prognosis prediction[4,5]. Recent studies indicate that TG variability, independent of mean concentration, is a more reliable predictor of incident AP, emphasizing the pathogenic role of lipid dynamics. Furthermore, the inability of standard lipid-lowering treatments, such as insulin or plasmapheresis, to consistently reduce organ failure or shorten hospitalization suggests that TG serves as a precursor rather than the primary driver of the condition[6,7]. The metabolic cascade likely depends on downstream metabolites, such as non-esterified fatty acids (NEFAs) or specific lipid mediators[8]. Thus, lipid abundance alone cannot explain disease

[1]Clinical Laboratory of Integrative Medicine, First Affiliated Hospital of Dalian Medical University, Dalian, Liaoning, China. [2]Department of Hepatobiliary and Pancreatic Surgery, General Surgery Center, First Hospital of Jilin University, Changchun, Jilin, China. [3]Department of Vascular Surgery, First Affiliated Hospital of Dalian Medical University, Dalian, China. [4]Department of Hepatobiliary Surgery, Chifeng Municipal Hospital, Chifeng, Inner Mongolia, China. [5]iPhenome Biotechnology Inc. Dalian (Yun Pu Kang), Dalian, Liaoning, China. [6]Department of Clinical Laboratory Medicine, First Affiliated Hospital of Dalian Medical University, Dalian, China. [7]Department of Otorhinolaryngology, Renmin Hospital of Wuhan University, Wuhan, Hubei, China. [8]These authors contributed equally: Anliang Huang, Qihang Yuan, Junhong Chen, Lei Wang. ✉e-mail: jicharles@126.com; rm003860@whu.edu.cn; shangdongdalian@163.com; shangdong@dmu.edu.cn; yinperry@126.com; yinpeiyuan@dmu.edu.cn

heterogeneity; rather, structural features and metabolic network properties likely govern the progression from metabolic dysfunction to acute inflammation.

Untargeted lipidomics offers a comprehensive view of metabolic changes, yet traditional analytical methods often treat lipid species as isolated entities[9,10]. Approaches like differential expression analysis or random forests (RFs) frequently overlook the intrinsic connectivity determined by chemical similarity and metabolic transformation. In high-dimensional clinical datasets with limited sample sizes, these topology-agnostic methods may fail to capture systemic network disturbances caused by altered enzymatic activities. Integrating chemical informatics with metabolic topology may provide a more detailed approach to understanding lipidomic dysregulation. Recently, artificial intelligence has been increasingly used to develop predictive models for severe AP (SAP) or HLAP. However, most existing models rely on conventional machine learning algorithms (e.g., RF, XGBoost) that process standard clinical biomarkers or one-dimensional omics data[11–13]. These traditional methods treat lipid species or clinical indices as independent variables, inherently failing to account for the complex topological interdependencies within metabolic networks. Unlike simple lipid accumulation, HLAP is characterized by widespread network perturbations. Therefore, there is a critical need to move from "abundance-centric" models to "network-aware" architectures in order to more accurately decipher the structural lipotoxicity at play.

Graph Neural Networks (GNNs) are highly effective for processing non-Euclidean data structures. While GNN architectures have been successfully applied to molecular graphs for predicting compound toxicity and bioactivity in drug discovery[14–16], their application in clinical lipidomics is still emerging. Network medicine theory suggests that disease phenotypes arise not from isolated molecular deficiencies but from topological disturbances within functional modules[17,18]. Building on this concept, it is hypothesized that modeling lipidomic profiles as graphs that encode chemical and metabolic relationships will reveal pathogenic signatures that conventional statistical methods may overlook.

This study introduces DeepLipiDecipher, a deep graph learning framework designed to reconstruct lipid metabolic networks using public knowledge bases to improve feature extraction. To validate this approach, the model was applied to a four-class clinical cohort consisting of healthy controls (Ctrl), HTG, AP, and hypertriglyceridemic pancreatitis (HLAP). DeepLipiDecipher demonstrated strong performance in this multi-class task, going beyond basic classification to accurately identify high-risk pathological states within a complex metabolic context. Specifically, it successfully isolated the distinct pathogenic lipid signature of HLAP from the noise of simple metabolic abnormalities (e.g., HTG) and non-lipid inflammation (e.g., AP). Subsequent feature importance analysis indicated a potential link between the HLAP phenotype and lipids involved in the SMPD3-Ceramide-PTGS2 axis.

Results

Clinical heterogeneity of HLAP and construction of the knowledge-guided lipidomic graph

The study design and workflow are illustrated in Fig. 1. A retrospective cohort of 433 subjects was enrolled, categorized into four distinct groups according to clinical guidelines: Healthy Controls (Ctrl, $n = 100$), HTG ($n = 124$), AP ($n = 123$), and HLAP ($n = 86$) (Table 1). Baseline characterization revealed a similar metabolic profile between the HTG and HLAP groups, both showing elevated body mass index (BMI > 27 kg/m^2) and a male predominance (>74%). Paradoxically, despite the HTG group exhibiting slightly higher median serum TG levels compared to the HLAP group (12.27 vs 10.64 mmol/L), their inflammatory landscapes diverged significantly. Correlation analysis between serum TG and C-reactive protein (CRP) (Supplementary Fig. S1A) demonstrated a distinct non-linear relationship. While HTG and HLAP patients overlapped along the lipid concentration axis, they segregated sharply by inflammatory response, with the HLAP group displaying profound inflammation (median CRP 117.04 mg/L) compared to the quiescent HTG group (5.11 mg/L). These results suggest that absolute lipid concentration alone does not explain the disparate HLAP risk, pointing to microstructural lipid heterogeneity as the key determinant, thereby justifying the use of our structure-aware DeepLipiDecipher algorithm.

To uncover the latent lipid signatures of HLAP, untargeted lipidomic profiling was performed across all subjects, quantifying 477 distinct lipid species (Fig. 2A, B). The detected lipidome spanned 13 major classes, predominantly consisting of TG ($n = 121$) and phosphatidylcholines (PC, $n = 106$). Principal Component Analysis (PCA) revealed that the first principal component (PC1, explaining 50.1% of the variance) effectively separated healthy controls from disease states. However, the HTG, AP, and HLAP groups exhibited substantial topological overlap in the two-dimensional embedding space (Fig. 2C), suggesting that gross lipid abundance profiles are insufficient to resolve disease subtypes. Stacked area plots further highlighted this redundancy, revealing that both HTG and HLAP groups showed a marked increase in relative TG abundance, coupled with a compensatory reduction in membrane phospholipids compared to controls (Fig. 2D), following a similar trajectory. Intersection analysis of upregulated lipids (Supplementary Fig. S1B) supported this observation; ~90% (188/209) of the lipids enriched in HLAP were shared with the HTG group, leaving only a small 5% fraction as HLAP-specific. This high degree of lipid similarity highlights the limitations of conventional differential expression analysis in distinguishing between simple metabolic accumulation and acute inflammation. Detailed statistical results, including fold changes and p-values for all pairwise differential lipidomic comparisons across the four cohorts, are provided in Supplementary Tables 1–6.

Global lipid expression profiles and fold-change patterns across multiple groups were comprehensively illustrated using Z-score normalized heatmaps and multiple comparison jitter plots (Supplementary Figs. S2, S3). The Mfuzz time-series clustering algorithm was further employed to investigate longitudinal lipidomic variation throughout disease progression, from controls to HTG, AP, and HLAP. This analysis identified two lipid clusters strongly associated with disease progression: one demonstrating a progressive increase in abundance with disease severity (Specific Increase) and another showing a progressive decrease (Specific Decrease) (Supplementary Fig. S4A). To assess the clinical relevance of these abundance trajectories, Spearman correlation analyses (Supplementary Fig. S4B) were performed between the two lipid clusters and key baseline patient characteristics, including diagnostic and prognostic markers such as CRP, WBC, TG, blood glucose, and serum amylase.

The results revealed distinct associations between lipid dynamics and clinical phenotypes. Specifically, within the progressively increasing cluster, representative molecules (e.g., PC(34:2)_PC(18:2/16:0) and Cer(36:1)_Cer(18:1/18:0)) showed significant positive correlations ($P < 0.001$) with indicators of systemic inflammation (CRP, WBC) and tissue injury (amylase), along with negative correlations with serum calcium levels. This pattern corresponds to the clinical features of severe pancreatitis, characterized by heightened inflammation and hypocalcemia. Conversely, within the progressively decreasing cluster, molecules (e.g., LysoPC(18:2) and PC(36:5)_PC(16:0/20:5)) exhibited significant negative correlations with inflammatory and tissue injury markers, while positively correlating with homeostasis indicators like serum calcium.

Synthesizing findings from cross-sectional and longitudinal analyses, changes in overall lipid abundance provide a macroscopic reflection of disease progression. However, for complex phenotypes like HTG and HLAP, which share highly overlapping inter-individual lipid distributions, reliance on one-dimensional abundance data alone lacks sufficient discriminatory power for accurate subtyping. This limitation prompted the shift from traditional abundance-centric models to graph-based approaches, incorporating prior knowledge such as chemical structures and metabolic pathways to capture more specific classification features at the micro-topological level.

Building on these insights, a hybrid graph was constructed, integrating lipid chemical structure and metabolic relationships to move beyond simple abundance metrics. Using a custom structural resolution strategy and

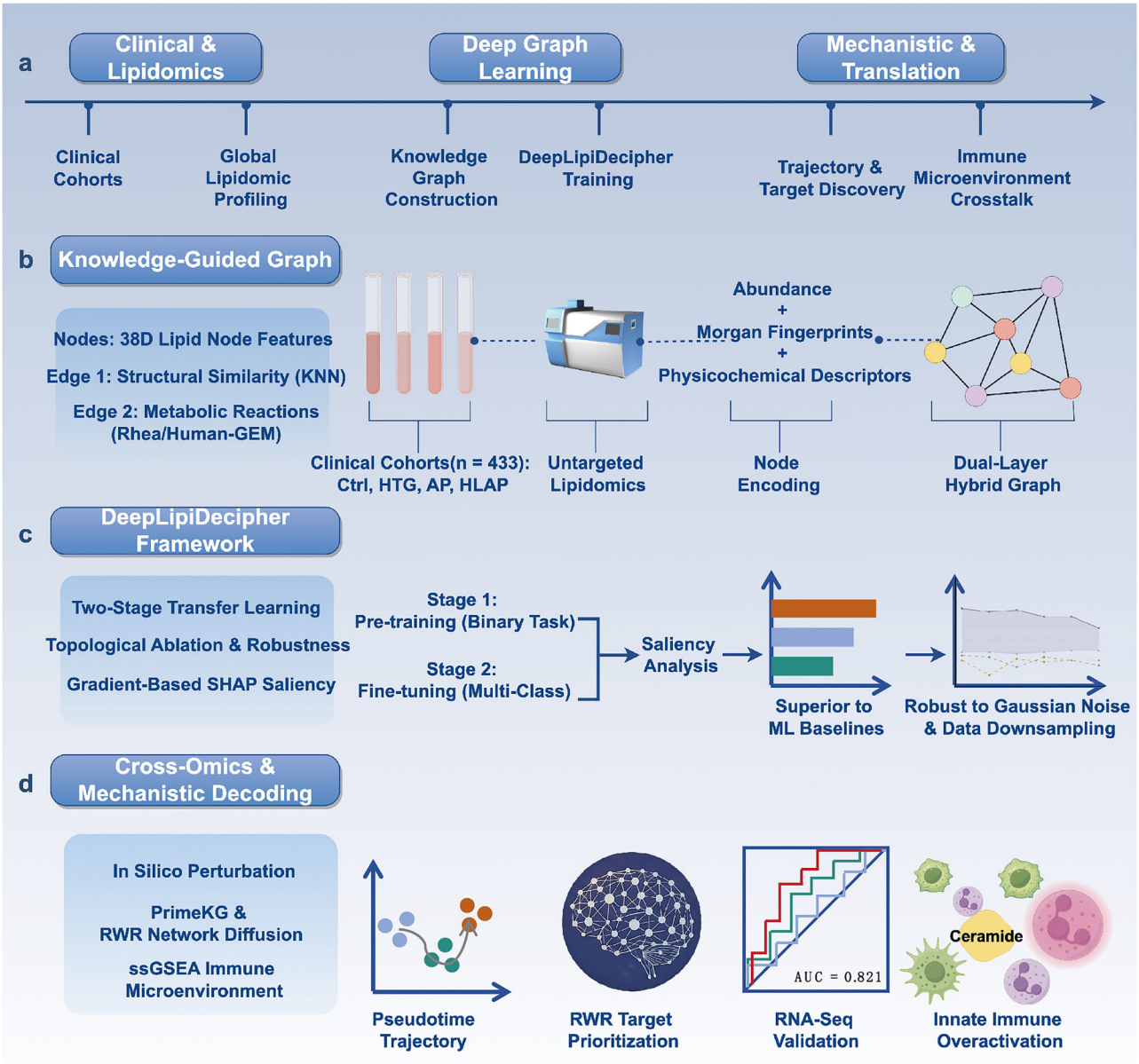


Fig. 1 | Overview of the study design and the DeepLipiDecipher analytical framework. a The complete research workflow, encompassing clinical lipidomics, knowledge graph construction, deep graph learning, and mechanistic translation. **b** Creation of the knowledge-guided hybrid lipidomic graph. Untargeted lipidomic profiling was conducted on a retrospective cohort of 433 subjects from four clinical groups (Ctrl, HTG, AP, HLAP). The hybrid graph integrates 38-dimensional node features (including abundance, Morgan fingerprints, and physicochemical descriptors) and edges based on structural similarity (KNN) and metabolic reactions (Rhea/Human-GEM). **c** The DeepLipiDecipher framework pipeline. The model utilizes a two-stage transfer learning approach (initial binary pre-training followed by multi-class fine-tuning), demonstrating superior performance and resilience to noise and data downsampling when compared to traditional machine learning methods, with gradient-based SHAP saliency analysis for feature interpretation. **d** Cross-omics and mechanistic decoding. This stage combines in silico network perturbation, PrimeKG-based Random Walk with Restart (RWR) target prioritization, and RNA-Seq transcriptomic validation to define pseudotime trajectories and reveal overactivation of the innate immune microenvironment (e.g., ceramide-driven crosstalk). Figure was created using the online platform Figdraw (Copyright Code: UYSYI95098).

metabolic reconstruction pipeline, the 477 lipid nodes were modeled into a topological network based on molecular structural similarity (KNN layer) and metabolic pathways (Fig. 2E), with attributes such as carbon chain length and degree of unsaturation embedded. Chemical space mapping via t-SNE visualized the clustering of lipid molecules (Fig. 2F). Superimposing Log_2 Fold Change (Log_2FC) values relative to controls onto this graph (Fig. 2G) revealed that specific TG and phospholipid sub-clusters exhibited a progressive surge in abundance (highlighted red regions) as the disease progressed from HTG to HLAP. This coordinated variation within local topological neighborhoods provides the structural foundation for DeepLipiDecipher to uncover potential pathogenic patterns.

In parallel, the global physicochemical properties of the lipidome were systematically characterized. Distribution analysis of Average Chain Length (ACL) and Average Double Bonds (ADB) (Fig. 2H, I) revealed that both HTG and HLAP groups had a significantly higher proportion of long-chain and polyunsaturated lipids compared to the Ctrl and AP cohorts ($P < 0.001$). While the overall distributions of HTG and HLAP overlapped, the HLAP group displayed a notably higher density within the high-unsaturation spectrum. These physicochemical shifts reflect fundamental alterations in membrane lipid composition, serving as key input features for the DeepLipiDecipher model to identify disease-specific signatures.

Table 1 | Baseline clinical characteristics

	Control	HTG	AP	HLAP	*P*-value
Number	100	124	123	86	
Age (years) (mean (SD))	45.00 (4.94)	40.32 (4.01)	51.44 (14.97)	41.20 (7.33)	<0.01
Sex (%)					<0.01
Female	46 (46.0)	30 (24.2)	54 (43.9)	22 (25.6)	
Male	54 (54.0)	94 (75.8)	69 (56.1)	64 (74.4)	
BMI (kg/m^2) (mean (SD))	22.49 (1.55)	28.96 (1.86)	23.89 (1.85)	27.40 (2.21)	<0.01
Triglycerides (mmol/L) (median [IQR])	1.21 [1.10, 1.32]	12.27 [10.82, 13.63]	1.61 [1.25, 1.91]	10.64 [8.20, 13.66]	<0.01
Total Cholesterol (mmol/L) (median [IQR])	4.50 [4.24, 4.82]	5.84 [5.46, 6.15]	4.67 [4.16, 5.13]	6.02 [5.38, 6.78]	<0.01
Fasting Glucose (mmol/L) (median [IQR])	5.14 [4.87, 5.52]	7.49 [6.78, 8.35]	6.81 [5.91, 7.76]	8.33 [6.67, 10.19]	<0.01
C-reactive Protein (mg/L) (median [IQR])	1.88 [1.48, 2.41]	5.11 [3.92, 6.10]	80.84 [63.00, 99.65]	117.04 [95.98, 142.04]	<0.01
White Blood Cells (×10^9/L) (mean (SD))	5.99 (0.76)	7.51 (0.98)	12.22 (4.43)	14.35 (4.41)	<0.01
Amylase (U/L) (median [IQR])	58.91 [49.09, 66.48]	72.94 [63.82, 80.29]	542.79 [222.50, 821.94]	463.79 [291.19, 599.29]	<0.01

Superior classification performance and topological robustness of the DeepLipiDecipher framework

To assess the efficacy of GNNs in decoding complex lipidomic data, the core prediction algorithm of DeepLipiDecipher, termed LipiGNN, was benchmarked against three mainstream machine learning models using global mean pooling (SVM, RF, XGBoost). Quantitative analysis on an independent test set evaluated comprehensive accuracy, clinical subtype resolution, interpretability, and resilience to interference. The results (Fig. 3A) showed that DeepLipiDecipher achieved an overall accuracy of 82.8% on the test set, significantly outperforming baseline models, which achieved accuracies ranging from 48% to 50%. In terms of the Matthews Correlation Coefficient (MCC), a robust measure of multi-class classification performance, DeepLipiDecipher scored ~0.78, while all baseline models fell below 0.3, indicating highly consistent predictions as opposed to random outcomes. Receiver Operating Characteristic (ROC) analysis (Fig. 3B) revealed that DeepLipiDecipher reached an Area Under the Curve (AUC) of 0.810, far surpassing XGBoost (0.515), RF (0.563), and SVM (0.603). This substantial AUC advantage highlights DeepLipiDecipher's ability to maintain a robust True Positive Rate across varying thresholds, effectively addressing the classification challenges faced by traditional models when working with high-dimensional lipid data.

Given that HLAP lipid abundance profiles are often masked by the background of severe HTG, accurately distinguishing the HLAP phenotype within this highly similar metabolic context became a critical challenge for validating whether the model captures the underlying pathogenic essence. To evaluate this, the model's detection capability for HLAP was assessed via the confusion matrix (Fig. 3C). The analysis revealed that DeepLipiDecipher achieved a Recall of 76% for HLAP patients, demonstrating superior disease detection capability. In contrast, baseline models exhibited significant limitations: SVM, XGBoost, and RF recorded extremely low recall rates for HLAP (6%, 18%, and 18%, respectively). The confusion matrices clearly indicated that these baseline models misclassified the majority of HLAP samples as HTG. This strongly supports the notion that traditional linear methods, based solely on lipid abundance, fail to distinguish HLAP from HTG, whereas DeepLipiDecipher, by integrating topological information, successfully captured the HLAP-specific lipid network configuration hidden beneath the abundance data, enabling precise identification of this high-risk phenotype.

To quantify the specific contribution of graph topology to predictive performance, ablation studies were conducted (Fig. 3D). Removing all edges, effectively reducing the model to a Multi-Layer Perceptron (MLP) that relies solely on node features, resulted in a sharp decline in classification accuracy to 69.0%. This indicates that inter-lipid relational information carries crucial classification features beyond individual lipid abundance. Further segmentation analysis revealed that removing metabolic reaction edges or chemical structural similarity edges (KNN) reduced accuracy to 73.6% and 71.3%, respectively. These findings highlight the dual sources of DeepLipiDecipher's performance: structural clustering features based on chemical fingerprints provide a foundational classification framework, while metabolic network priors refine the model's decision boundaries, enhancing its discriminatory power.

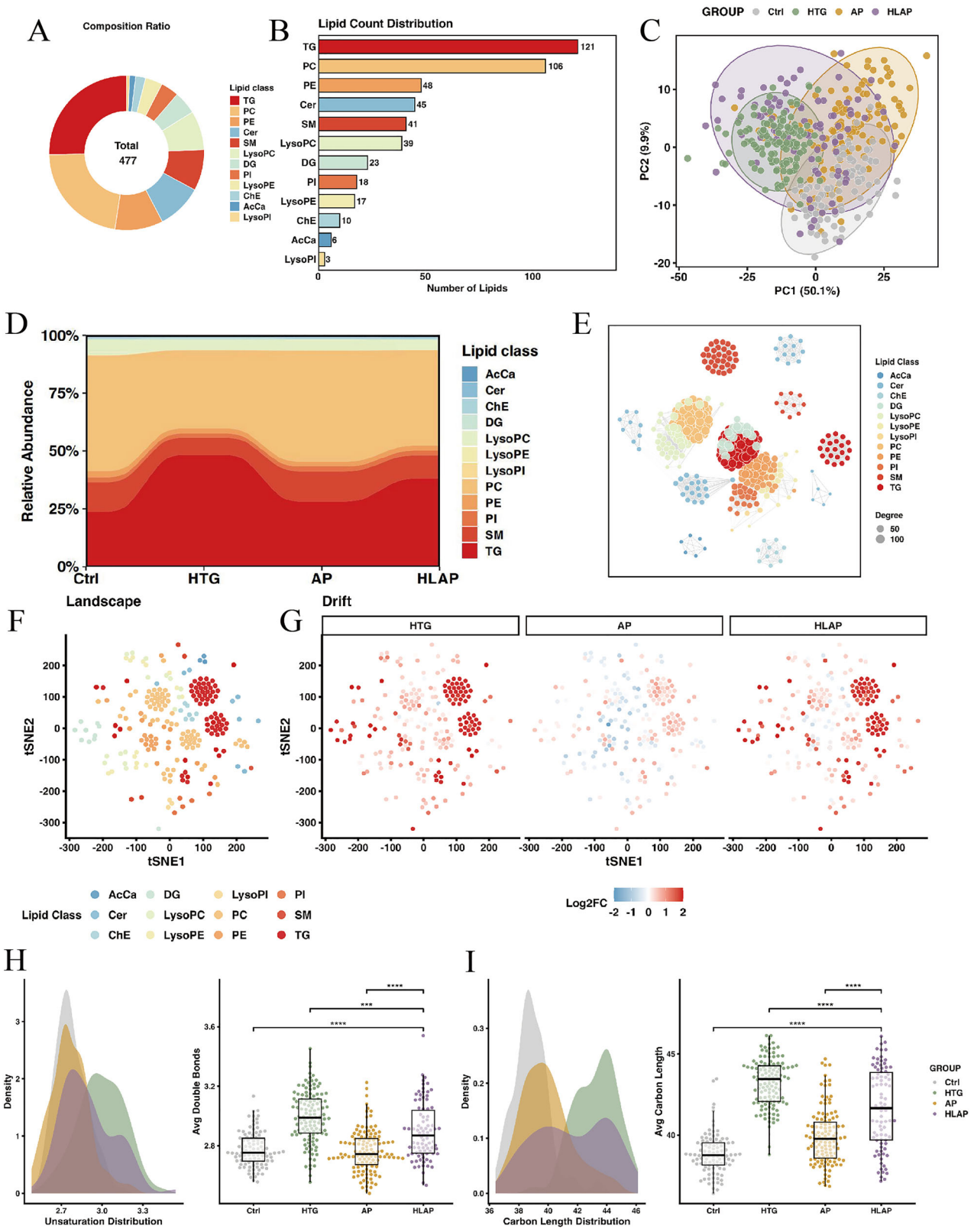
Training dynamics analysis (Fig. 3E) revealed strong convergence for DeepLipiDecipher, with test set accuracy surpassing 75% after ~20 epochs. The consistent decline in Cross-Entropy Loss, without significant overfitting, suggests that graph structure regularization effectively constrains the model's search space. Data efficiency evaluation (Fig. 3F) further demonstrated DeepLipiDecipher's advantage in small-sample settings: using only 40% of the training data, test accuracy remained around 75%, significantly outperforming baseline models that used the full dataset. In contrast, XGBoost, RF, and SVM showed minimal improvement in performance with increased data volume, remaining at 40%–50%, highlighting the limitations of traditional models in feature extraction when processing high-dimensional, sparse data.

To assess model stability under non-ideal clinical conditions, random noise was injected into input features to simulate potential measurement errors or biological fluctuations (Fig. 3G). The results showed that even with 50% noise intensity, DeepLipiDecipher maintained classification accuracy around 68%, demonstrating substantial resilience. While some baseline models exhibited minor fluctuations under noise, their accuracy remained consistently low. This strongly indicates that DeepLipiDecipher does not rely solely on the absolute abundance of specific lipid molecules, which are susceptible to noise, but rather leverages robust topological structural features within the lipid network, thus enhancing the model's generalization capability in real-world data.

Dynamic lipidomic evolution and structural-phenotypic associations in disease progression

Utilizing manifold learning and multi-scale structural resolution, the dynamic lipidomic trajectory from healthy controls to HLAP was reconstructed, systematically analyzing the molecular alterations driving this pathological process. UMAP-based manifold projection (Fig. 4A) illustrated the continuous distribution of samples in latent space, clearly delineating a unidirectional trajectory from the control group (Ctrl) through HTG and AP, ultimately evolving toward HLAP. Pseudotime analysis further quantified this progression, showing that the HLAP group is situated at the terminal end of the evolutionary trajectory (Pseudotime >0.8) and is significantly separated from other groups. This distribution suggests that HLAP is not merely an exacerbation of AP but represents a distinct pathological state with unique metabolic-inflammatory characteristics, following a specific lipid evolutionary pattern.

To decouple the complex pathological drivers of HLAP, a pattern recognition strategy based on multi-condition logical discrimination was



employed (Fig. 4B), identifying two distinct lipid alteration patterns that reveal a dual driving mechanism for disease pathogenesis. The first pattern, termed Synergistic Aggravation, involves specific TG and ceramide (Cer) subclasses, which exhibit an initial elevation during the HTG stage, followed by an exponential surge (continuous rise in Log_2FC) in the HLAP stage. This trend suggests the cumulative effect of metabolic load, positioning these lipids as potential pathophysiological substrates for disease onset. The second pattern, termed Unique Rebound, features a non-monotonic "V-shaped" variation. Certain lipids, such as LysoPC and specific PE ether lipids, show significantly reduced levels in the general AP group (likely due to inflammatory consumption) but exhibit a remarkable resurgence in the HLAP group. This atypical kinetic behavior implies that HLAP patients may

Fig. 2 | Global lipidomic landscape and construction of the knowledge-guided structural-metabolic graph. Composition ratio (**A**) and absolute count distribution (**B**) of the 477 identified lipid species across 13 major lipid classes. **C** Principal Component Analysis (PCA) score plot of the four clinical cohorts. Ellipses indicate 95% confidence intervals. Note the considerable overlap in lipid profiles between the HTG and HLAP groups. **D** Stacked area chart illustrating the dynamic changes in the relative abundance of major lipid classes throughout disease progression (from Ctrl to HLAP), emphasizing the substantial increase in TG and the compensatory decrease in phospholipids. **E** The constructed hybrid topological network, integrating 477 lipid nodes. Edges represent both molecular structural similarity (KNN) and metabolic reaction pathways. Node size reflects connectivity, and lipid classes are color-coded. **F** t-SNE projection mapping the chemical space of the lipidome, showing the distribution of clusters colored by lipid classes. **G** t-SNE abundance drift maps illustrating the Log_2 Fold Change (Log_2FC) of lipid levels in HTG, AP, and HLAP groups compared to the Ctrl group. Red indicates upregulation, while blue denotes downregulation. Density distribution plots and boxplots characterizing the global physicochemical shifts: **H** Average Double Bonds (ADB, indicating unsaturation) and **I** Average Carbon Chain Length (ACL) across the four cohorts. Boxplots display the median and interquartile range. Statistical significance was assessed using appropriate comparative tests (***$P < 0.001$, ****$P < 0.0001$).

possess unique lipid remodeling or compensatory mechanisms, distinct from the metabolic consumption processes typically observed in general pancreatitis.

To further elucidate the molecular basis of these phenotypic patterns, the latent features captured by the GNN were mapped into interpretable structural motifs and validated across chemical structure, physical properties, and clinical function dimensions. Structural enrichment analysis (Fig. 4C) provided definitive molecular evidence for HLAP specificity: among HLAP-associated lipids, there was significant enrichment of vinyl ether linkages (Vinyl Ether Plasmalogen, OR > 4.0) and conjugated dienes (Conjugated Diene, OR > 10.0). Notably, the substantial presence of conjugated dienes (hallmarks of polyunsaturated fatty acid (PUFA) peroxidation) directly confirms the occurrence of intense lipid peroxidation (LPO) reactions in HLAP patients, which may underlie cellular injury.

Multidimensional characterization of physicochemical properties (Fig. 4D) further revealed the functional fingerprints of key motifs. The analysis indicated that Motif 7 and Motif 9 exhibited maximal activation in the HLAP group, though each possessed distinct characteristics: Motif 9, primarily associated with lower molecular weight and low hydrophobicity, showed a highly significant positive correlation with serum TG and blood glucose levels ($P < 0.001$). This suggests that specific small-molecule or highly water-soluble lipid derivatives may exhibit anomalous activity under severe metabolic load. In contrast, Motif 7 displayed unique chemical attributes, with Z-scores indicating exceptionally high Topological Polar Surface Area (TPSA) and Hydrogen Bond Acceptors ($P < 0.05$). More importantly, Motif 7 demonstrated no significant correlation with total TG mass but was positively correlated with systemic inflammatory markers such as CRP and WBC (Fig. 4E). This multidimensional association indicates that the structural features represented by Motif 7 (high polarity, oxidative modification, and ether bond structure) may play a more direct role in the HLAP inflammatory cascade than simple lipid abundance. This provides a molecular explanation for the clinical observation where disease severity does not always correlate with TG levels in some patients, highlighting the importance of lipid microstructural toxicity over total lipid quantity when assessing HLAP risk. To this end, deconstructed lipid faceted lollipop plots were also used to offer a structure-specific metabolic perspective across dimensions of carbon chain length and saturation (Supplementary Fig. S5).

Network-based driver identification and cross-omics decoding

To identify the lipid features most crucial for HLAP prediction, a feature perturbation-based sensitivity analysis was conducted (Fig. 5A). Virtual knockout of specific lipid features led to a significant reduction in the model's predicted probability for HLAP (x-axis). In some cases, perturbing these individual features was enough to alter the final classification, reversing predictions where samples initially classified as HLAP were reclassified into non-severe categories. Notably, the virtual removal of DG(36:2)_DG(18:1/18:1) and PE(40:6)_PE(18:0/22:6) not only decreased predicted probabilities but also caused classification reversals in 18.6% and 17.4% of HLAP samples, respectively. Interestingly, removing lipids with high absolute abundance in the HLAP group had minimal impact on the model's output. This suggests that DeepLipiDecipher does not rely solely on the cumulative concentration of individual molecules but instead identifies specific non-linear lipid combinatorial patterns.

Using the PrimeKG knowledge base, a cross-omics regulatory network was constructed (Fig. 5B) to map key pathogenic lipids to potential upstream regulatory genes. Topological analysis revealed three hub genes with high centrality: PTGS2 (COX-2), SMPD3 (nSMase2), and NR5A2 (LRH-1). Functional annotation (Fig. 5C) showed that SMPD3 is a critical node in sphingolipid metabolism (regulating the conversion of SM to Cer), NR5A2 functions as a metabolism-associated nuclear receptor, and PTGS2 serves as a core enzyme driving inflammation and LPO.

Metabolic network analysis (Fig. 5D) revealed latent abnormalities in metabolic flux. The SMase (sphingomyelinase) and SMS (sphingomyelin synthase) nodes displayed high betweenness centrality within the network. A marked imbalance in the substrate-to-product ratios of related metabolic reactions was observed in the HLAP group, suggesting dysregulation of the SMPD3/SMase-mediated pathway. This disruption in the homeostasis of SM and Cer facilitates the stress-induced accumulation of pro-inflammatory ceramides, aligning with the lipid transition marker features captured by the model.

Synthesizing these multi-scale analyses, a "Two-Hit" pathogenic mechanism for HLAP is proposed. The first "hit" involves dysregulation of key enzymes like SMPD3, leading to the stress-induced accumulation of sphingolipids such as ceramides, which induces basal cytotoxicity. The second "hit" occurs with the hyperactivation of the central network hub PTGS2 (COX-2), which drives intense LPO. This causal pathway offers a robust explanation for the substantial enrichment of "Conjugated Dienes" observed in (Fig. 4C). These high-polarity, oxidatively modified lipids, catalyzed by PTGS2, serve as the "fuse" for systemic inflammation. This immunometabolic cascade provides a novel molecular framework for HLAP pathogenesis, independent of total TG mass, and strongly suggests that targeting SMPD3 and PTGS2 may offer therapeutic potential to block HLAP's malignant progression.

Expression dynamics of core lipid metabolic targets and their potential associations with the immune microenvironment and cell death

To further assess the translational relevance of core lipid metabolic regulatory programs during AP exacerbation, this study incorporated an independent high-throughput RNA-Seq peripheral blood cohort (GSE194331). The selection of validation targets integrated cross-omics network topological features with macroscopic lipidomic phenotypes. In addition to the computationally identified hub genes PTGS2 and SMPD3, the critical enzyme ACSL4 was also included in the candidate validation set. This choice was based on the previously observed enrichment of LPO markers, such as conjugated dienes, in the HLAP lipidome, as ACSL4 catalyzes the transmembrane insertion of PUFAs, serving as substrates for this peroxidation reaction. Although NR5A2, identified as a metabolic hub in the preceding network analysis, primarily exhibits hepato-pancreatic parenchymal-specific expression, its low basal transcriptional level in peripheral immune cells led to its exclusion from the validation phase during the data quality control (QC) process. Consequently, NR5A2 was not included in this evaluation. This section focused on analyzing the expression dynamics of ACSL4, SMPD3, and PTGS2 during clinical exacerbation and

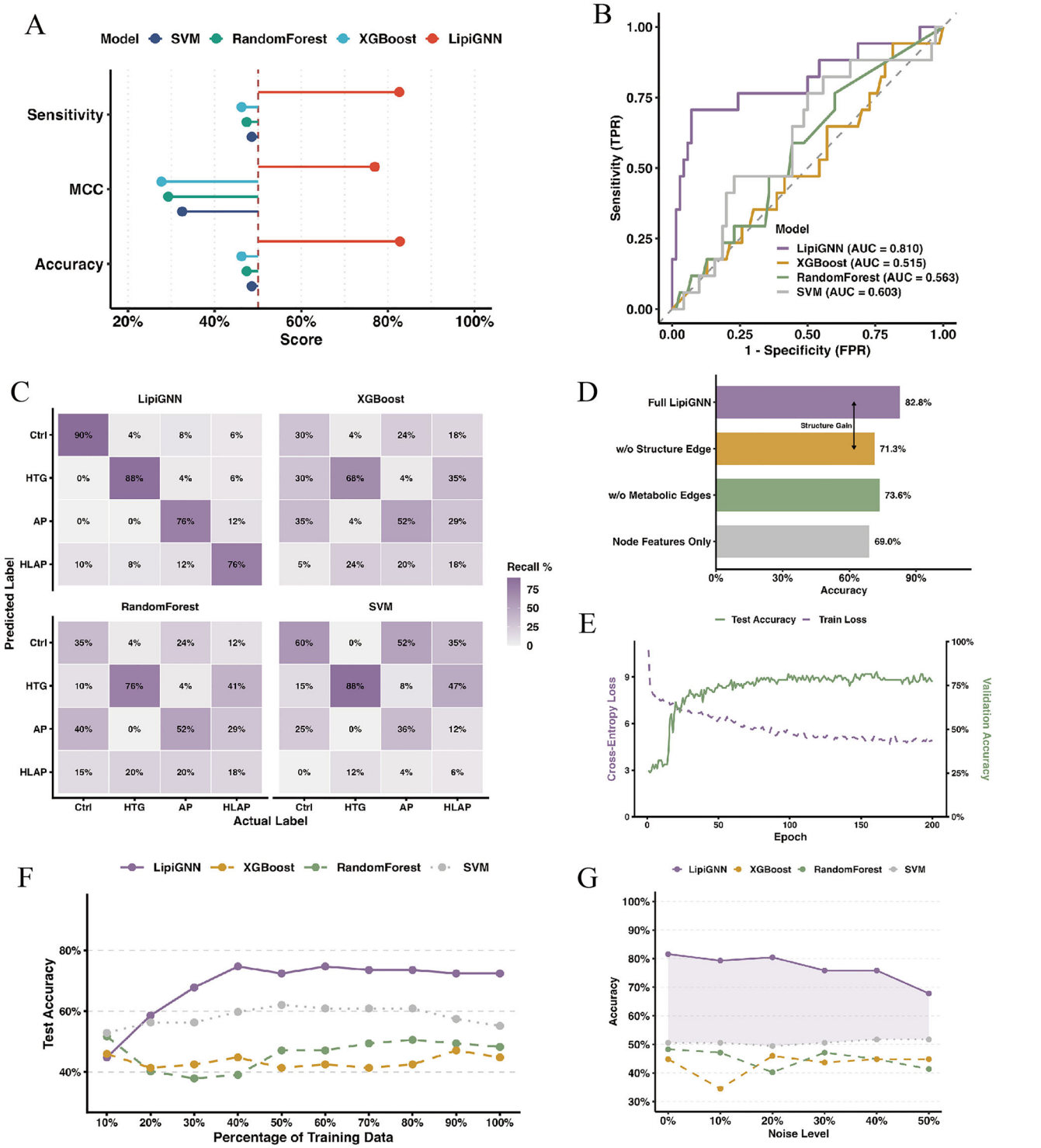


Fig. 3 | Superior classification performance and topological robustness of the DeepLipiDecipher framework. A Quantitative comparison of LipiGNN (the core algorithmic engine of the DeepLipiDecipher framework) with three standard machine learning baseline models (SVM, Random Forest, XGBoost) based on Sensitivity, Matthews Correlation Coefficient (MCC), and overall Accuracy on the independent test set. **B** Receiver Operating Characteristic (ROC) curves showcasing the diagnostic performance. DeepLipiDecipher achieves a superior Area Under the Curve (AUC) of 0.810, significantly outperforming linear baseline models. **C** Confusion matrices assessing the ability to differentiate specific clinical subtypes. DeepLipiDecipher successfully penetrates the metabolic noise of HTG to achieve a 76% recall rate for the high-risk HLAP phenotype, while baseline models frequently misclassify HLAP as HTG. **D** Ablation study quantifying the contribution of graph topology to predictive accuracy. Removal of chemical structure edges, metabolic reaction edges, or all edges (reducing the model to a Node Features Only MLP) leads to a progressive decline in performance, highlighting the importance of topological structure. **E** Training dynamics of DeepLipiDecipher, showing rapid convergence of validation accuracy (solid green line) and a steady decrease in training cross-entropy loss (dashed purple line) over 200 epochs. **F** Data efficiency evaluation under data-limited scenarios. DeepLipiDecipher maintains robust test accuracy (>75%) using only 40% of the training data, greatly outperforming baseline models trained on the full dataset. **G** Stress testing evaluating model resilience to data perturbations. DeepLipiDecipher retains high classification accuracy (~68%) even with 50% simulated feature noise, demonstrating its reliance on robust network topology rather than isolated lipid abundances.

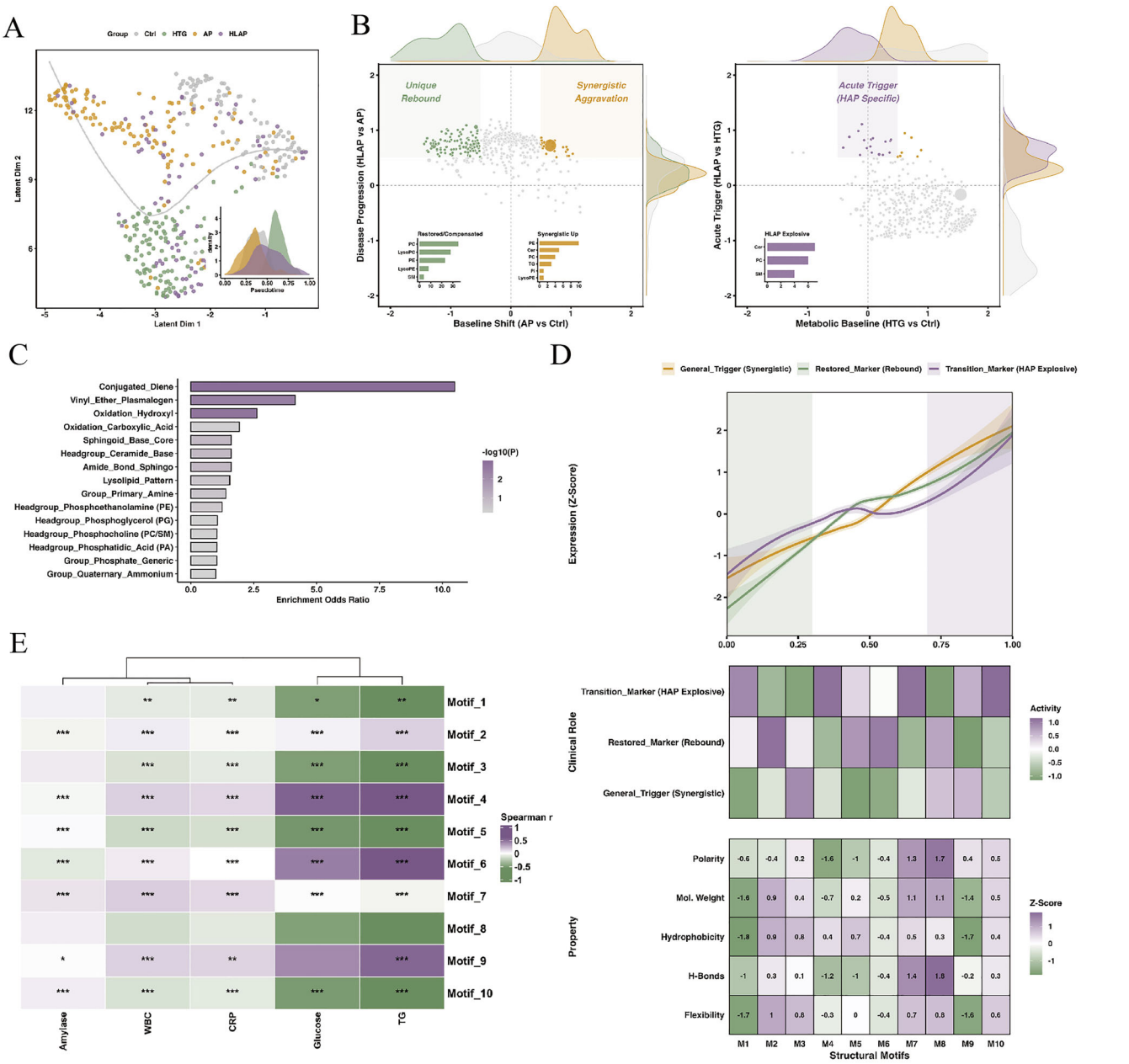


Fig. 4 | Dynamic lipidomic evolution and structural-phenotypic associations during HLAP progression. A UMAP-based manifold projection reconstructing the continuous pseudotemporal trajectory from healthy controls (Ctrl) to hypertriglyceridemic pancreatitis (HLAP). The solid gray line delineates the principal evolutionary path. The inset density plot shows the distribution of pseudotime across cohorts, indicating that HLAP is located at the terminal stage of the pathological progression. **B** Multi-condition logical pattern recognition identifying complex lipid drivers. Scatter plots reveal distinct lipid kinetic patterns based on baseline and progression shifts: Synergistic Aggravation (orange, continuous exponential increase), Unique Rebound (green, V-shaped non-monotonic variation), and Acute Trigger/HLAP Explosive (purple, HLAP-specific abrupt emergence). Inserted bar charts outline the primary lipid classes contributing to each pattern. **C** Structural enrichment analysis of HLAP-associated lipids. Bar lengths represent enrichment odds ratios, with colors indicating statistical significance (-log10 *P*-value). Notable enrichment is observed in oxidative modification products (Conjugated Dienes) and ether linkages (Vinyl Ether Plasmalogens). **D** Multidimensional characterization of lipid structural motifs. The top panel illustrates the standardized expression dynamics (Z-score) of the three identified marker roles (Synergistic, Rebound, and Explosive) along the pseudotime axis. The middle and bottom heatmaps quantify the activation of ten specific structural motifs (M1-M10) across the clinical roles and their corresponding physicochemical properties (e.g., Polarity, Molecular Weight, Hydrogen Bonds). **E** Heatmap showing Spearman rank correlations between the functional activities of Motifs 1–10 and core clinical parameters. Notably, Motif_9 strongly correlates with metabolic load (TG, Glucose), while Motif_7, characterized by high polarity and oxidation modifications (as shown in D), is significantly correlated with systemic inflammatory markers (CRP, WBC), independent of absolute lipid mass. (*$P < 0.05$, **$P < 0.01$, ***$P < 0.001$).

their correlation with the immune microenvironment and programmed cell death (PCD) pathways.

Expression alterations of these target genes were significantly associated with the clinical progression of AP. Specifically, compared to healthy controls, ACSL4 expression was significantly upregulated in the peripheral blood of SAP patients, while SMPD3 and PTGS2 were significantly downregulated (Fig. 6A). Further trend analysis showed a progressive increase in ACSL4 expression from mild AP (MAP) to moderately severe AP (MSAP) to SAP ($R = 0.36$, $p < 0.001$), suggesting its potential role in disease exacerbation (Fig. 6B). In contrast, SMPD3 expression decreased

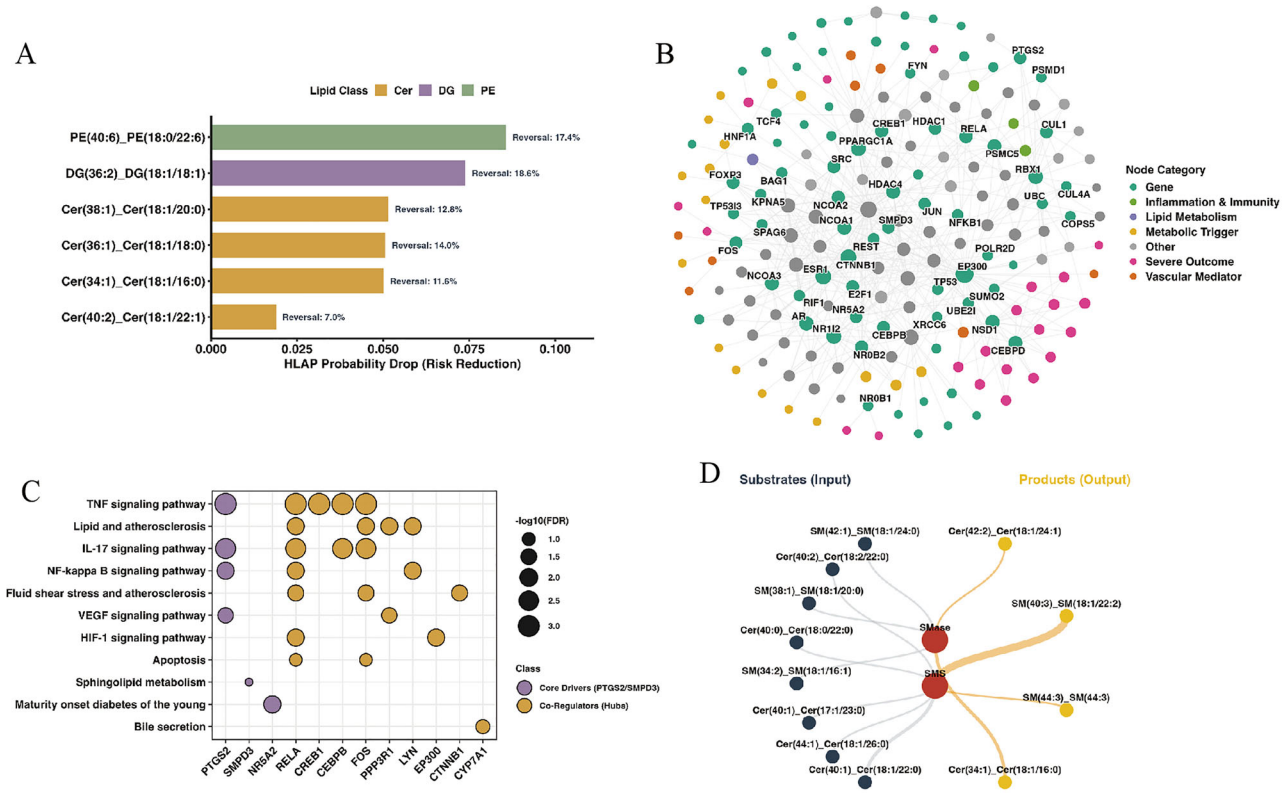


Fig. 5 | Network-based identification of core pathogenic drivers and cross-omics mechanistic decoding. A Feature perturbation-based sensitivity analysis identifying critical lipid drivers for HLAP prediction. The bar chart displays the absolute decrease in the DeepLipiDecipher model's predicted probability for HLAP following the virtual knockout of specific lipid features. Data labels represent the "Reversal" rate, which indicates the percentage of HLAP samples erroneously reclassified into non-severe categories after feature removal. **B** Cross-omics regulatory network constructed using the PrimeKG knowledge base, mapping key pathogenic lipids to their potential upstream regulatory genes. Nodes are color-coded by category (e.g., Genes, Inflammation & Immunity, Lipid Metabolism). Topological analysis highlights PTGS2, SMPD3, and NR5A2 as central hub genes linking lipid dysregulation to severe disease outcomes. **C** Functional pathway enrichment of the identified network hub genes. Bubble size represents statistical significance (-log10 FDR), and colors differentiate core drivers (PTGS2, SMPD3, purple) from co-regulatory hubs (gold). Notably, PTGS2 is linked to intense inflammatory and peroxidation signaling, while SMPD3 is associated with sphingolipid metabolism, supporting the "Two-Hit" pathogenic hypothesis. **D** Reconstructed local metabolic flux network focusing on Sphingomyelinase (SMase) and Sphingomyelin synthase (SMS). The bipartite-like graph depicts dysregulated metabolic transitions from substrate Sphingomyelins (SM, left) to product Ceramides (Cer, right) driven by SMPD3/SMase hyperactivation, highlighting the stress-induced accumulation of pro-inflammatory lipid species.

significantly with increasing disease severity ($R = -0.37$, $p < 0.001$), likely reflecting the attenuation of homeostatic mechanisms. PTGS2 also exhibited a marginal downward trend during disease progression ($p = 0.052$). Based on these expression patterns, the predictive value of ACSL4, SMPD3, and PTGS2 for SAP was further evaluated (Fig. 6C). ROC curve analysis indicated that individual genes had moderate predictive ability (AUC range: 0.683–0.701), whereas a combined model integrating all three genes achieved an AUC of 0.821, demonstrating strong clinical discriminatory power.

Given the frequent association between SAP progression, systemic inflammatory response syndrome (SIRS), and immune dysregulation, this study employed the ssGSEA algorithm to examine the correlations between the target genes and immune cell infiltration characteristics (Fig. 6D). The findings revealed distinct immune-related profiles for these genes. ACSL4 expression showed a significant positive correlation with the infiltration of pro-inflammatory innate immune cells, particularly macrophages and neutrophils ($p < 0.001$), while exhibiting a significant negative correlation with adaptive immune cell populations, including T cells, B cells, and NK cells. This pattern is consistent with the pathological phenotype of innate immune overactivation and lymphocyte depletion observed during SAP exacerbation. In contrast, SMPD3 expression positively correlated with adaptive immune cell populations, suggesting that its downregulation may be linked to immune homeostasis imbalance in severe patients. PTGS2 expression also exhibited a potential negative correlation trend with certain adaptive immune cells.

Given the frequent association of lipid metabolic disorders, particularly LPO, with specific PCD processes, the ssGSEA algorithm was further used to quantify the enrichment scores of various cell death pathways and assess their correlations with the core lipid genes (Fig. 6E). ACSL4 expression was significantly positively correlated with the enrichment of pro-inflammatory cell death pathways, including ferroptosis, PANoptosis, and pyroptosis. Scatter plot analysis demonstrated significant positive associations between ACSL4 and ferroptosis ($R = 0.53$, $p < 0.001$) and PANoptosis ($R = 0.56$, $p < 0.001$) (Fig. 6F), aligning with its role in LPO pathways. In contrast, SMPD3 expression showed significant negative correlations with PANoptosis ($R = -0.39$, $p < 0.001$) and pyroptosis ($R = -0.45$, $p < 0.001$), while PTGS2 also exhibited a negative correlation trend with disulfidptosis and necrosis (Fig. 6F). These results suggest that the aberrant expression of lipid-related genes is not only associated with lipid profile alterations but may also be linked to the activation of specific cell death pathways, such as ferroptosis and PANoptosis.

These results suggest that the transcriptomic remodeling of lipid metabolism, characterized by the upregulation of ACSL4 and the downregulation of SMPD3 and PTGS2, accompanies the clinical progression of AP. This transcriptional reconfiguration holds potential as a biomarker for poor prognosis in severe cases and may contribute to the transition of the immune microenvironment from a lymphocyte-dominated state to one

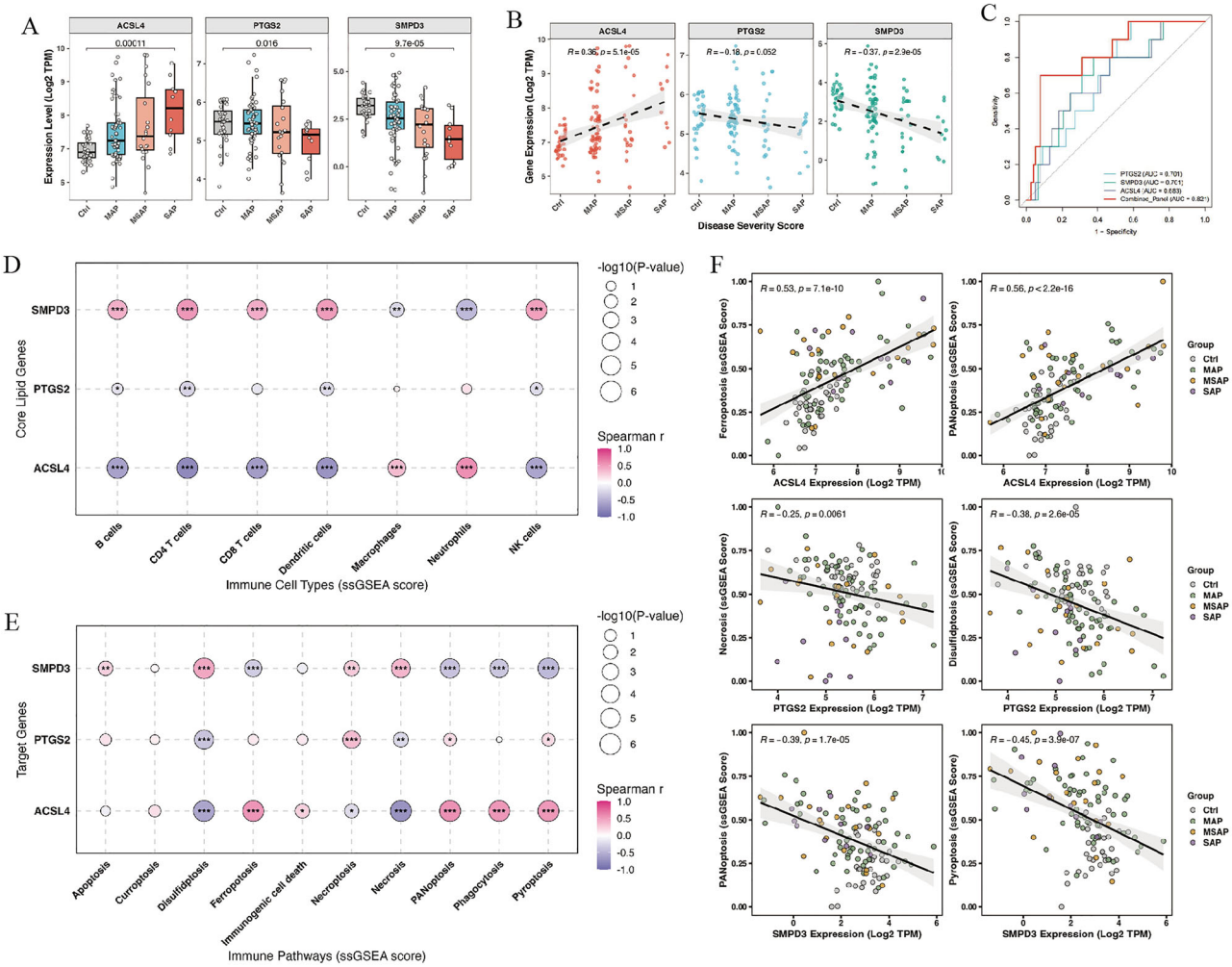


Fig. 6 | Expression dynamics of core lipid metabolic targets and their potential associations with the immune microenvironment and programmed cell death during the exacerbation of acute pancreatitis. A Boxplots depicting the transcriptional expression levels of core lipid metabolic genes (ACSL4, PTGS2, and SMPD3) across the clinical spectrum of acute pancreatitis (AP). Data are from the independent peripheral blood RNA-Seq cohort (GSE194331), covering healthy controls (Ctrl) to mild (MAP), moderately severe (MSAP), and severe AP (SAP). ACSL4 is significantly upregulated in SAP compared to the Ctrl group, while SMPD3 and PTGS2 are downregulated. **B** Scatter plots illustrating the linear regression trends of target gene expression (Log_2 CPM) with the exacerbation of AP. Dashed lines represent linear regression trends with 95% confidence intervals (shaded areas), and R denotes the Spearman correlation coefficient. ACSL4 shows a progressive upregulation trend, whereas SMPD3 demonstrates a significant downregulation trend. **C** Receiver Operating Characteristic (ROC) curves assessing the predictive value of these target genes for identifying SAP. Although individual genes show moderate predictive ability (AUC ranging from 0.683 to 0.701), the combined 3-gene diagnostic model (Combined Panel) achieves an AUC of 0.821, indicating clinically relevant discriminatory efficacy for severe outcomes. **D** Immune microenvironment associations. The bubble heatmap visualizes Spearman rank correlations between core lipid gene expression and the infiltration abundance of various immune cell populations (quantified via ssGSEA). Bubble size correlates with statistical significance (-log10 *P*-value), and color indicates the correlation coefficient (R; pink for positive, purple for negative). ACSL4 correlates positively with innate pro-inflammatory cells (e.g., macrophages, neutrophils) and negatively with adaptive immune cells (e.g., T cells, B cells, NK cells). **E** Bubble heatmap demonstrating correlations between target genes and the enrichment scores of programmed cell death pathways (ssGSEA). ACSL4 is significantly positively correlated with pro-inflammatory cell death modes, including ferroptosis, PANoptosis, and pyroptosis. **F** Scatter plots detailing specific significant correlations between individual core genes and representative cell death pathways. ACSL4 is positively associated with ferroptosis and PANoptosis scores, while SMPD3 shows negative associations with PANoptosis and pyroptosis. (Significance levels for heatmaps: $^{*}P < 0.05$, $^{**}P < 0.01$, $^{***}P < 0.001$).

dominated by inflammatory macrophages and neutrophils. Additionally, it may influence specific inflammatory cell death pathways, which are closely associated with disease exacerbation.

Discussion

This study presents DeepLipiDecipher, a knowledge-driven GNN framework designed to unravel the complex lipidomic landscape of HLAP. Beyond simple disease classification, our analysis delves into the metabolic and immune regulatory networks, highlighting a potential SMPD3-Ceramide-PTGS2 metabolic-inflammatory crosstalk axis in disease pathogenesis. This work represents a shift from traditional abundance-based models to network topology analysis, offering a fresh perspective for understanding the pathophysiology of this complex clinical condition.

Conventional lipidomic studies primarily focus on linear differential abundance. Recent efforts have integrated lipidomic and metabolic features with machine learning to build predictive models for SAP, demonstrating the superiority of multivariate pattern recognition over single biomarkers[19]. Despite these advancements, however, considerable overlap in lipid abundance profiles between HLAP and HTG patients was observed, limiting the discriminatory power of conventional machine learning models based on linear separability. To overcome this challenge, DeepLipiDecipher incorporates topological information from non-Euclidean space, using the

inductive bias of graph structures to guide model learning. This biologically informed deep learning approach, which integrates metabolic reactions and chemical similarities, aligns with the "Biologically Informed AI" or "Gray-Box Modeling" paradigm, known for enhancing generalization in small-sample, high-dimensional biological datasets[20,21].

The model utilizes a dual-layer graph structure to identify biologically significant "functional modules." Unlike standard enrichment methods that treat molecules in isolation[22,23], DeepLipiDecipher models the topological dependencies of lipids within the metabolic network. As previously suggested, coordinated variations in these modules often reflect systemic perturbations in key enzymes like SMPD3 or MBOAT7. The GNN's message-passing mechanism performs "network smoothing" and "denoising" by aggregating neighborhood information, implicitly inferring the functional state of these enzymes and capturing system-level signals that traditional statistical methods might miss[24,25].

Theoretically, disease phenotypes arise not from isolated abundance changes but from topological disruptions in molecular networks. Our approach links genetic or environmental stressors to observable lipid network perturbations, bridging the genotype-phenotype gap. Additionally, the impressive data efficiency of DeepLipiDecipher highlights the advantage of GNNs in processing high-dimensional omics data with limited sample sizes, addressing the "curse of dimensionality" often encountered in clinical research[26–29].

A key clinical contribution of this study is resolving the "HTG Paradox" that has long posed a challenge in risk stratification. Our findings suggest that acinar cell fate is governed not by total TG mass, but by the "structural toxicity" of the lipidome. DeepLipiDecipher revealed a distinct HLAP lipid signature characterized by the synergistic accumulation of highly unsaturated lipids and ether-bond modifications. This discovery aligns with recent mechanistic insights into lipotoxicity, which indicate that NEFAs—especially PUFAs—generated after lipolysis are the key effectors of inflammation and tissue damage, rather than inert TGs themselves[8,30–32].

This specific "lipid configuration shift" transitions the cell membrane from a relatively stable, inert state to a highly vulnerable one, hypersensitive to oxidative stress. While ether lipids are traditionally considered antioxidants that preserve membrane stability[33,34], their abnormal accumulation in the pathological context of HLAP—particularly plasmalogens enriched with PUFA side chains—likely reflects a failure in adaptive membrane remodeling. These PUFA-containing phospholipids can promote the formation of membrane microdomains and alter membrane physical properties, disrupting normal transmembrane signal transduction. Therefore, the lipid configuration shift in HLAP patients indicates that the membrane's Peroxidizability Index has surpassed its antioxidant defense capacity, particularly under metabolic stress.

These findings support the "Fuel-Fuse" hypothesis: while HTG provides the metabolic substrate ("fuel"), an inflammatory storm is only triggered when the lipidome adopts a high-risk configuration—the high-unsaturation, oxidation-prone "fuse." This mechanistic insight suggests that clinical risk assessments should evolve beyond monitoring TG levels, favoring composite biomarkers that incorporate lipid structural features.

Interpretability analysis further clarified the molecular mechanisms underlying the ignition of this "fuse." The transition markers identified by DeepLipiDecipher are not only enriched in Motif 7-associated, highly polar SM and Cer but also show a distinct trend toward chain elongation and polyunsaturation. This remodeling of the lipid profile goes beyond altering membrane fluidity; it lays the biophysical groundwork for ferroptosis.

The observed enrichment of PUFAs, particularly the accumulation of arachidonic acid (AA) or adrenic acid (AdA) side chains in phosphatidylethanolamines (PE), mirrors the membrane remodeling driven by ACSL4 (Acyl-CoA Synthetase Long-Chain Family Member 4)[35,36]. ACSL4 specifically activates and integrates free PUFAs into membrane phospholipids, creating a pool of PL-PUFA substrates highly vulnerable to oxidative damage[37,38]. In the oxidative stress environment of HLAP, these unstable membrane lipids breach the antioxidant defense threshold of GPX4, initiating an irreversible LPO cascade[39–42].

In this context, the concurrent enrichment of ether lipids in the transition markers does not merely serve as a passive bystander but acts as an amplifier of this lethal environment. Ether lipids provide additional PUFA donors for membrane lipid synthesis, contributing synergistically to a highly "combustible" membrane landscape that propagates ferroptotic signaling[43]. Consequently, the lipid profile identified by DeepLipiDecipher, characterized by high PUFA-containing PE (PUFA-PE) and elevated ether lipids, forms a functional "Pro-Ferroptotic Lipid Fingerprint." This finding provides a molecular explanation for the susceptibility of HLAP patients to severe acinar cell necrosis and the release of damage-associated molecular patterns (DAMPs), fueling a vicious cycle of lipolysis, ferroptosis, inflammation, and organ injury[44,45]. Furthermore, it suggests that targeting ACSL4 or inhibiting LPO may represent promising intervention strategies to halt HLAP progression.

Cross-omics network inference highlights the central role of the sphingolipid metabolic pathway in the pathogenesis of HLAP. SMPD3 (nSMase2) emerges as a critical node in the constructed network, suggesting that disrupted metabolic flux facilitates the conversion of sphingomyelin to ceramide. This metabolic disturbance likely disrupts the balance between ceramide and sphingosine-1-phosphate[46–48]. Existing evidence implicates the pathological accumulation of ceramides, induced by a lipotoxic environment, as a key driver of mitochondrial dysfunction. Similar to mechanisms observed in metabolic liver disease, excessive ceramide accumulation may exacerbate necrotic acinar cell death by inhibiting mitophagy, a crucial protective mechanism during AP[46,49–51]. Furthermore, ceramide metabolism is linked to lysosomal instability and endoplasmic reticulum stress[52,53], with downstream enzymes like ASAH1 potentially contributing to the aberrant activation of trypsinogen[54]. These findings suggest that HLAP patients experience an SMPD3-mediated metabolic aberration that not only promotes the cytotoxic accumulation of ceramide but also initiates organelle dysfunction, offering a metabolic explanation for the non-linear relationship between TG fluctuations and local pancreatic injury[8,55,56].

The identification of hub genes within the network reveals a potential connection between metabolic pathways and inflammatory responses, providing insight into why HLAP patients exhibit a more pronounced systemic inflammatory response (e.g., elevated CRP) compared to HTG. PTGS2 (COX-2), as an inflammation-associated node, is positioned within the network, with its correlation to the accumulation of Motif 7-associated lipids. Our analysis suggests that ceramides may function not only as intracellular metabolites but also as "metabolic-immune" signaling molecules, playing a role in immune cell phenotypic transformation. Prior studies have demonstrated that sphingolipid metabolic remodeling can promote macrophage polarization toward a pro-inflammatory M1 phenotype and amplify inflammatory responses via STAT3 or NF-κB signaling pathways[57,58]. In this context, PTGS2 may act as a downstream regulator, responding to TLR4 or NLRP3 inflammasome signals mediated by ceramides, thereby contributing to prostaglandin synthesis and the release of inflammatory factors. This hypothesis aligns with our KEGG pathway enrichment results (TNF signaling) and literature reports regarding increased pyroptosis in HTG-AP[59].

This network-topology-based "metabolic-immune" association hypothesis is further supported by the analysis of an independent transcriptomic cohort (GSE194331). The data reveal that transcriptional changes—characterized by significant upregulation of ACSL4 and marked downregulation of SMPD3—correlate with shifts in the immune microenvironment during the progression of SAP. Elevated ACSL4 expression correlates with increased infiltration of innate immune cells, such as neutrophils and macrophages, while decreased SMPD3 expression is associated with a reduced proportion of adaptive immune cells, including T and B cells. This transition from a lymphocyte-dominated homeostatic state to a myeloid-dominated inflammatory state may represent a key pathophysiological feature of SAP complicated by SIRS.

Transcriptomic analysis further suggests a potential link between lipid metabolic remodeling and PCD mechanisms. Specifically, upregulation of ACSL4 is positively correlated with ferroptosis scores and exhibits a

synergistic increase alongside pyroptosis and PANoptosis scores[60–63]. This may be mechanistically related to ACSL4-mediated LPO, which compromises cell membrane integrity. The subsequent release of DAMPs and reactive oxygen species (ROS) likely serves as upstream signals, indirectly activating the NLRP3 inflammasome and RIPK3 pathways. This, in turn, promotes the assembly of the PANoptosome and related cascade reactions within the inflammatory microenvironment of SAP[64,65].

Clinical cohort data further reveal that SMPD3 (nSMase2) expression decreases as the disease progresses to a severe stage, correlating with increased pyroptosis and PANoptosis scores. While previous studies have indicated that ceramide accumulation can promote pro-death effects in certain parenchymal cells[66], the downregulation of SMPD3 in peripheral immune cells may reflect alterations in microenvironmental metabolic adaptability[67,68]. Reduced SMPD3 activity could disrupt specific pathways of ceramide synthesis, redirecting lipid flux and increasing the generation of potentially cytotoxic lipids, such as lysophospholipids or oxidized phospholipids. These metabolites may serve as endogenous stress signals, contributing to inflammasome activation and influencing immune cell status, thus exacerbating the development of SIRS[59].

Synchronous analysis reveals that PTGS2 (COX-2)[60], a key marker gene for ferroptosis and LPO, exhibits a downregulation trend during the severe stage of SAP, coinciding with increased scores for necrosis and disulfidptosis. This suggests that oxidative stress and microcirculatory disturbances in the severe stage impair the metabolic and transcriptional functions of peripheral immune cells[62]. Decompensation of antioxidant transcription factors, such as Nrf2, and alterations in energy metabolism may not only restrict the continuous transcription of PTGS2[69] but also establish a microenvironment conducive to novel forms of cell death driven by insufficient glucose uptake and disulfide bond accumulation (e.g., disulfidptosis). These findings highlight the importance of integrating lipid metabolic networks (such as ACSL4 and SMPD3 nodes) with immune cell metabolic remodeling and PCD pathways when exploring the pathological mechanisms of severe pancreatitis, such as HLAP. This approach may provide new insights for potential clinical interventions.

Finally, certain core lipids, including those associated with Motif 7, show a positive correlation with systemic inflammatory markers (CRP, WBC), suggesting that these lipid molecules may influence the immune-inflammatory injury cascade at the clinical level. The central role of the nuclear receptor NR5A2 (LRH-1) within the network further suggests that a specific lipid environment might modulate the sensitivity of acinar and immune cells to metabolic stress by regulating the "lipid-nuclear receptor-inflammation" axis.

From a clinical translation standpoint, the DeepLipiDecipher framework establishes a practical paradigm for precision risk stratification and therapeutic intervention. In future clinical practice, upon the admission of a patient with severe HTG, clinicians could integrate rapid lipidomic profiling with the model to calculate a composite Lipotoxicity Risk Score. Unlike the reliance on total TG levels, which often perpetuates the HTG paradox, this model evaluates specific structural drivers of pathogenesis, such as the accumulation of PUFA-PE and ceramide. Patients identified with a high-risk lipidomic network topology could then be prioritized for immediate intensive care and early interventions, including lipid-lowering apheresis or therapies targeting LPO (e.g., ACSL4 or PTGS2 inhibitors). In contrast, patients with a low-risk lipid profile could avoid unnecessary invasive treatments. By guiding such tailored clinical decisions, this model holds the potential to optimize resource allocation, prevent irreversible systemic organ failure, and ultimately improve outcomes in HLAP patients.

Despite the strong mechanistic hypotheses provided, several limitations merit consideration. First, the graph construction is limited by the completeness of current knowledge bases, such as Rhea and HMDB, which may omit novel lipid metabolic pathways or uncharacterized molecular species. Second, the proposed mechanisms, including the SMPD3-Ceramide-PTGS2 axis, are largely inferred computationally and require rigorous biological validation via gene-edited animal models or organoid systems. Finally, given that this study is retrospective, future multi-center prospective cohort studies are essential to assess the model's generalizability and clinical applicability.

In conclusion, the DeepLipiDecipher framework highlights the potential of artificial intelligence in deciphering complex lipidomic data. By elucidating the topological features of the lipidome, this study offers novel insights into the pathogenesis of HALP and lays the groundwork for the development of precision diagnostic and therapeutic strategies.

Methods

Study population and experimental design

A clinical cohort of 433 subjects was enrolled in this study, with the protocol approved by the Ethics Committee of Chifeng Municipal Hospital (Ethics No: CK2023004). Written informed consent was obtained from all participants prior to inclusion. The subjects were categorized into four groups based on the Revised Atlanta Classification (2012) and admission lipid profiles: Healthy Controls (Ctrl, $n = 100$), with no history of pancreatic disease and serum TG < 1.7 mmol/L; HTG ($n = 124$), defined by serum TG ≥ 5.7 mmol/L in the absence of AP; AP ($n = 123$), meeting standard diagnostic criteria (typical abdominal pain, amylase/lipase >3× the upper limit of normal, and radiological evidence), primarily of biliary or idiopathic etiology; and HLAP ($n = 86$), meeting AP criteria with concurrent TG ≥ 11.3 mmol/L (or >5.65 mmol/L with lactescent serum), excluding other etiologies such as gallstones. Exclusion criteria included chronic pancreatitis, pancreatic malignancy, pregnancy, and incomplete clinical data. Clinical trial registration: Not applicable.

Sample preparation and UHPLC-MS/MS

Lipidomics analysis, lipid extraction, and untargeted profiling. Lipids were extracted using a methyl tert-butyl ether (MTBE) liquid-liquid extraction protocol. Briefly, 20 µL of serum was homogenized with 120 µL of methanol containing internal standards by vortexing at 1000 rpm for 5 min. Phase separation was induced by adding 360 µL MTBE and 100 µL ultrapure water, followed by vortexing for 10 min and a 10-minute incubation at room temperature. After centrifugation at 4 °C (13,000 × *g*, 15 min), the upper organic phase was collected and lyophilized. The dried lipid residue was reconstituted in 80 µL of acetonitrile-isopropanol (1:1, v/v) prior to analysis. QC samples, prepared by pooling equal aliquots of all biological samples, were interspersed throughout the analytical run to monitor system stability.

Lipidomic profiling was performed using a UPLC-HRMS platform, consisting of a Thermo Scientific Ultimate™ 3000 system coupled to a Q Exactive™ Quadrupole-Orbitrap mass spectrometer. Chromatographic separation was achieved with an Accucore C30 core-shell column, using a binary mobile phase system: Solvent A (60% acetonitrile in water) and Solvent B (90% isopropanol/10% acetonitrile), both modified with ammonium formate and 0.1% formic acid. The gradient elution started at 10% B, linearly increased to 50% B over 5 min, and reached 100% B by 23 min. Mass spectrometry data were acquired in Full Scan mode using a heated electrospray ionization (H-ESI) source operating in both positive and negative polarities. Source parameters included a sheath gas flow of 45 arb, an auxiliary gas flow of 10 arb, a capillary temperature of 320 °C, a heater temperature of 355 °C, and an S-Lens RF level of 55.

Data preprocessing

Raw mass spectra were processed using TraceFinder software (Thermo Scientific) for peak extraction, retention time alignment, and integration. Lipid identification was based on accurate precursor m/z and MS/MS fragmentation patterns, generating a raw abundance matrix. To mitigate batch effects and normalize input distribution, missing values were imputed using the half-minimum method (50% of the minimum non-zero value per feature). Abundances exceeding 10^3 were $\log_2$-transformed to compress the dynamic range, followed by Z-score standardization to ensure uniform feature weighting.

Longitudinal lipid trajectory clustering and clinical phenotype correlation

To capture the macroscopic dynamic trajectories of the lipidome across successive stages of disease progression, fuzzy c-means clustering was applied using the Mfuzz R package. Group-averaged lipid abundances were Z-score standardized to facilitate the algorithm's identification of lipid clusters exhibiting progressive accumulation or depletion in line with the increasing severity of the disease. To assess the clinical relevance of these dynamic trajectories, core baseline clinical and biochemical indices, including CRP, white blood cell count (WBC), serum TG, blood glucose, and serum amylase, were extracted. Spearman's rank correlation was performed to systematically map associations between the abundance of representative core lipid molecules within these clusters and the aforementioned clinical phenotypes.

Lipid chemical structure resolution

Lipid species were annotated using the SwissLipids and LipidMaps databases, prioritizing HMDB ID matching. A normalization strategy was employed for text-based annotation to resolve nomenclature variations, including the removal of isomer tags (e.g., n3/n6) and standardization of plasmalogen prefixes (P-/O-). A rule-based reannotation algorithm was applied to correct structural misclassifications, automatically remapping diacyl-phospholipids containing null acyl chains (e.g., "PC 16:0/0:0") to their corresponding lysophospholipid counterparts (e.g., "LPC 16:0"). For lipids without exact structural matches, a nearest-neighbor imputation approach identified the optimal surrogate within the same lipid class by minimizing a weighted chemical distance $D = \Delta C + 5 \times \Delta DB$, where ΔC and ΔDB represent differences in carbon number and double bond count, respectively. A strict threshold ($\Delta C \leq 2$, $\Delta DB \leq 1$) ensured physicochemical fidelity, defaulting to the closest chain-length representative if no proxy met these criteria.

Hybrid graph construction and feature encoding

To model the intricate lipid interactome, each patient's lipid profile was treated as an attributed graph G=(V,E). Nodes (C) represented individual lipid species, encoded as 38-dimensional feature vectors integrating standardized abundance (1 dimension), 32 principal components derived from 2048-bit Morgan fingerprints (radius = 2), and 5 key physicochemical descriptors (molecular weight, LogP, rotatable bonds, TPSA, and hydrogen bond acceptors). The graph topology (E) was defined by a dual-layer network: a chemical similarity layer connecting nodes to their k = 5 nearest structural neighbors via Jaccard distance, and a metabolic reaction layer linking substrate-product pairs (Tanimoto similarity >0.5) based on Rhea and Human-GEM ontologies.

Deep graph learning architecture and training protocol

The DeepLipiDecipher framework was developed with LipiGNN as its core classification engine, a GNN designed to decode disease states from the constructed lipid graphs. The model was trained using a two-stage transfer learning strategy. Initially, it was pre-trained on a binary classification task (healthy vs. disease) for 30 epochs using cross-entropy loss with label smoothing ($\epsilon = 0.1$). It was then fine-tuned for the four-class classification (Ctrl, HTG, AP, HLAP) over 200 epochs. To address class imbalance, weighted cross-entropy loss was employed, assigning a 1.5× weight to the HLAP class. Optimization was performed using AdamW with a cosine annealing learning rate schedule (initial learning rate = 10^{-3}). The dataset was split into an 80:20 training-test ratio.

Baseline comparison and ablation study

The performance of DeepLipiDecipher was benchmarked against classic machine learning algorithms, including RF, Support Vector Machine (SVM), and XGBoost. To ensure a fair comparison and isolate the contribution of graph topology, baseline models used global mean-pooled features derived from the graph nodes. All models underwent stratified 5-fold cross-validation on the training set, with final evaluation conducted on the hold-out test set using accuracy, weighted F1-score, MCC, and AUROC.

To dissect the contribution of topological components, an ablation study was performed with three variants: (1) removing chemical similarity edges (w/o Structure Edges), (2) removing metabolic reaction edges (w/o Metabolic Edges), and (3) removing all edges, reducing the GNN to a node-based MLP. This systematic degradation allowed quantification of the specific predictive value contributed by chemical and metabolic connectivity.

Robustness and feature importance analysis

Model robustness was evaluated through stress testing, where Gaussian noise of varying intensities ($\lambda\sigma$, where $\lambda \in [0.1, 0.5]$) was injected into test set features to assess performance decay. Data efficiency was analyzed by incrementally downsampling the training set from 100% to 10%. To identify the key drivers of HLAP prediction, gradient-based saliency analysis was employed. The feature importance score I_i for each node i was calculated as the L1 norm of the element-wise product of the input feature and its gradient:

$$I_i = \sum \left| \nabla_{Xi} S_{HAP} \odot X_i \right|$$

where $\nabla_{Xi} S_{HAP}$ denotes the gradient of the HLAP class score with respect to the node feature vector X_i. Scores were averaged across all HLAP patients and normalized to yield a Global GNN Importance ranking.

Multi-scale chemo-structural and trajectory analysis

High-importance lipids underwent multi-scale analysis. Chemically, structural motifs were identified using RDKit, with enrichment assessed via Fisher's exact test ($P < 0.05$). Correlations between GNN importance scores and physicochemical descriptors (e.g., oxidation risk, membrane fluidity) were quantified using Spearman's rank correlation. Network-level "Metabolic Hubs" were defined as lipids exhibiting both high GNN importance and high betweenness centrality within the chemical similarity network (Tanimoto >0.7). Disease progression was modeled using Uniform Manifold Approximation and Projection (UMAP) to define a pseudotime trajectory along PC1. A sliding window approach was applied to analyze the dynamic evolution of physicochemical properties. Additionally, a logic-gated classifier categorized lipids into three functional classes: "Transition Markers" (specific to the HTG-to-HLAP transition), "Universal Triggers" (elevated in both AP and HLAP), and "Background Markers." The causal potential of top-ranked lipids was validated via in silico perturbation, where "virtual knockout" (zeroing features) of specific lipids was performed to measure the resultant drop in HLAP probability (ΔP_{HAP}).

Cross-omics network construction

To map lipids to genetic regulators, key lipid species were linked to interacting proteins via SwissLipids. Using the PrimeKG knowledge base, a network diffusion algorithm was executed, seeded with pancreatitis and HTG-associated genes, to define a "HLAP Genetic Core." Potential therapeutic targets were identified using a Random Walk with Restart (RWR) algorithm on the PrimeKG network, prioritizing genes within the restart set defined by the HLAP core and key lipid regulators. Functional annotation of gene modules was performed using hypergeometric distribution tests.

Independent transcriptomic validation and immune microenvironment profiling

To independently validate the transcriptional dynamics of core lipid metabolic genes, the peripheral blood RNA-sequencing dataset GSE194331 was retrieved from the Gene Expression Omnibus (GEO). This cohort comprises 87 patients with AP across varying severities (MAP, MSAP, and SAP) alongside 32 healthy controls. Raw count matrices were normalized to Transcripts Per Kilobase Million (TPM) and $\log_2$-transformed prior to downstream analysis. To decode the immunological crosstalk mediated by these metabolic targets, the single-sample Gene Set Enrichment Analysis

(ssGSEA) algorithm was employed. Utilizing a validated signature panel of 28 immune cell types, the relative infiltration abundances of specific innate (e.g., macrophages, neutrophils) and adaptive (e.g., T cells, B cells) immune populations within each sample were quantified. The interplay between core gene expression and immune infiltration patterns was subsequently evaluated using Spearman's rank correlation.

Data availability

The raw data can be obtained from the corresponding author upon reasonable request.

Code availability

The core implementations and a tutorial subset of the DeepLipiDecipher pipeline are publicly available on GitHub at https://github.com/AaronHwang8720/DeepLipiDecipher. Additional custom scripts or specific proprietary configurations used in this study are available from the corresponding author upon reasonable request.

Received: 12 November 2025; Accepted: 14 May 2026;
Published online: 27 May 2026

References

1. Ma, J. et al. Precision nutrition management in hyperlipidemia-associated acute pancreatitis: mechanistic insights and personalized therapeutic approaches. *Front. Nutr.* **12**, 1583889 (2025).
2. Malick, W. A., Do, R. & Rosenson, R. S. Severe hypertriglyceridemia: existing and emerging therapies. *Pharm. Ther.* **251**, 108544 (2023).
3. Patel, R. S. et al. Elevated plasma triglyceride concentration and risk of adverse clinical outcomes in 1.5 million people: a CALIBER linked electronic health record study. *Cardiovasc. Diabetol.* **21**, 102 (2022).
4. Tung, Y. C. et al. High triglyceride variability increases the risk of first attack of acute pancreatitis. *Am. J. Gastroenterol.* **118**, 1080–1090 (2023).
5. Deng, H. et al. Clinical outcomes in a multicenter cohort involving 919 patients with hypertriglyceridemia-associated acute pancreatitis. *Am. J. Gastroenterol.* **120**, 2405–2414 (2025).
6. Syed-Abdul, M. M., Tian, L., Hegele, R. A. & Lewis, G. F. Futility of plasmapheresis, insulin in normoglycaemic individuals, or heparin in the treatment of hypertriglyceridaemia-induced acute pancreatitis. *Lancet Diab. Endocrinol.* **13**, 528–536 (2025).
7. He, W. et al. Low-molecular-weight heparin plus insulin in hypertriglyceridemic acute pancreatitis: a randomized clinical trial. *JAMA Netw. Open* **8**, e2542124 (2025).
8. Rajalingamgari, P. et al. Prospective observational study and mechanistic evidence showing lipolysis of circulating triglycerides worsens hypertriglyceridemic acute pancreatitis. *J. Clin. Invest.* **135**, e184785 (2024).
9. Zhou, J. et al. Triglyceride-lowering therapies in hypertriglyceridemia-associated acute pancreatitis in China: a multicentre prospective cohort study. *BMC Med.* **22**, 535 (2024).
10. Zou, K., Liu, W., Xia, W. & Zhao, Y. Ferroptosis in hypertriglyceridemic acute pancreatitis: mechanisms and therapeutic implications. *J. Inflamm. Res.* **18**, 18115–18135 (2025).
11. Zhang, D. et al. Novel insight on marker genes and pathogenic peripheral neutrophil subtypes in acute pancreatitis. *Front. Immunol.* **13**, 964622 (2022).
12. Sun, Z. et al. Prediction of infected pancreatic necrosis in patients with acute necrotizing pancreatitis based on ensemble machine learning model. *World J. Emerg. Surg.* **20**, 69 (2025).
13. Critelli, B. et al. A systematic review of machine learning-based prognostic models for acute pancreatitis: Towards improving methods and reporting quality. *PLoS Med.* **22**, e1004432 (2025).
14. Ahmad, W., Chong, K. T. & Tayara, H. GGAS2SN: gated graph and SmilesToSeq network for solubility prediction. *J. Chem. Inf. Model* **64**, 7833–7843 (2024).
15. Peng, J., Fu, L., Yang, G. & Cao, D. Advanced AI-driven prediction of pregnancy-related adverse drug reactions. *J. Chem. Inf. Model* **64**, 9286–9298 (2024).
16. Zhang, Q., Wei, Y. & Liu, L. GraphPro: an interpretable graph neural network-based model for identifying promoters in multiple species. *Comput Biol. Med.* **180**, 108974 (2024).
17. Hang, S. & Hegele, R. A. The evaluation of plozasiran for the treatment of familial chylomicronemia syndrome. *Expert. Rev. Endocrinol. Metab.* **21**, 195–204 (2026).
18. Sikora Kessler, A. et al. Temporal patterns of triglyceride testing and test results among adults with severe or extreme hypertriglyceridemia in US clinical practice. *Am. J. Prev. Cardiol.* **24**, 101356 (2025).
19. Deng, D. et al. Non-invasive liquid biopsy based on metabolomic profiling improves diagnosis and early warning of severe acute pancreatitis. *NPJ Digit Med.* **9**, 116 (2026).
20. Yan, H. et al. Prior knowledge-guided multilevel graph neural network for tumor risk prediction and interpretation via multi-omics data integration. *Brief. Bioinform* **25**, bbae184 (2024).
21. Feng, J., Liang, Y. & Yu, T. MM-GANN-DDI: multimodal graph-agnostic neural networks for predicting drug-drug interaction events. *Comput Biol. Med.* **166**, 107492 (2023).
22. Mziou-Sallami, M. et al. GNNenrich: a novel method for pathway enrichment analysis based on graph neural network. *Bioinformatics* **41**, btaf478 (2025).
23. Cheng, Z., Xu, D., Ding, D. & Ding, Y. Prediction of drug-target interactions with high- quality negative samples and a network-based deep learning framework. *IEEE J. Biomed. Health Inf.* **29**, 1567–1578 (2025).
24. Wang, W., Zhang, X. & Dai, D. Q. DeFusion: a denoised network regularization framework for multi-omics integration. *Brief. Bioinform.* **22**, bbab057 (2021).
25. Zhang, X., Wang, W., Ren, C. X. & Dai, D. Q. Learning representation for multiple biological networks via a robust graph regularized integration approach. *Brief. Bioinform.* **23**, bbab409 (2022).
26. Xiao, S., Lin, H., Wang, C., Wang, S. & Rajapakse, J. C. Graph neural networks with multiple prior knowledge for multi-omics data analysis. *IEEE J. Biomed. Health Inf.* **27**, 4591–4600 (2023).
27. Li, Y., Wang, Y., Liang, T., Li, Y. & Du, W. A multi-omics integration framework using multi-label guided learning and multi-scale fusion. *Brief. Bioinform.* **26**, bbaf493 (2025).
28. Li, S., Hua, H. & Chen, S. Graph neural networks for single-cell omics data: a review of approaches and applications. *Brief. Bioinform.* **26**, bbaf109 (2025).
29. Lin, C. P. et al. MoAGNN: a multi-omics hierarchical graph neural network for subtype classification and prognosis prediction in lung adenocarcinoma. *Brief. Bioinform.* **27**, bbaf735 (2026).
30. de Bruin, C. R., de Bruijn, W. J. C., Hemelaar, M. A., Vincken, J. P. & Hennebelle, M. Separation of triacylglycerol (TAG) isomers by cyclic ion mobility mass spectrometry. *Talanta* **281**, 126804 (2025).
31. Goh, M. W. S. & Tero, R. Non-raft submicron domain formation in cholesterol-containing lipid bilayers induced by polyunsaturated phosphatidylethanolamine. *Colloids Surf. B Biointerfaces* **210**, 112235 (2022).
32. Hansen, S. E. J., Varbo, A., Nordestgaard, B. G. & Langsted, A. Hypertriglyceridemia-associated pancreatitis: new concepts and potential mechanisms. *Clin. Chem.* **69**, 1132–1144 (2023).
33. Obis, E. et al. Lipidomic alterations in the cerebral cortex and white matter in sporadic Alzheimer's disease. *Aging Dis.* **14**, 1887–1916 (2023).
34. Oh, S. et al. Non-bioenergetic roles of mitochondrial GPD2 promote tumor progression. *Theranostics* **13**, 438–457 (2023).
35. Ding, K. et al. Acyl-CoA synthase ACSL4: an essential target in ferroptosis and fatty acid metabolism. *Chin. Med J.* **136**, 2521–2537 (2023).

36. Merkel, M. et al. Mitochondrial reactive oxygen species formation determines ACSL4/LPCAT2-mediated ferroptosis. *Antioxidants* **12**, 1590 (2023).
37. Zhang, H. L. et al. PKCβII phosphorylates ACSL4 to amplify lipid peroxidation to induce ferroptosis. *Nat. Cell Biol.* **24**, 88–98 (2022).
38. Xu, W., Deng, K. & Pei, L. P4HA3 depletion induces ferroptosis and inhibits colorectal cancer growth by stabilizing ACSL4 mRNA. *Biochem. Pharm.* **233**, 116746 (2025).
39. Capella, G. et al. Lipid metabolism and ferroptosis resistance in dormant breast cancer cells: emerging therapeutic vulnerabilities. *Diagnostics* **16**, 667 (2026).
40. Li, Y., Li, Z., Ran, Q. & Wang, P. Sterols in ferroptosis: from molecular mechanisms to therapeutic strategies. *Trends Mol. Med.* **31**, 36–49 (2025).
41. Duo, K. et al. Ferroptosis inhibitors: mechanisms of action and therapeutic potential. *Cell Mol. Life Sci.* **82**, 441 (2025).
42. Beatty, A. et al. Ferroptotic cell death triggered by conjugated linolenic acids is mediated by ACSL1. *Nat. Commun.* **12**, 2244 (2021).
43. Sokol, K. H. et al. Lipid availability influences ferroptosis sensitivity in cancer cells by regulating polyunsaturated fatty acid trafficking. *Cell Chem. Biol.* **32**, 408–422.e6 (2025).
44. Peng, Q. et al. IDH2-NADPH pathway protects against acute pancreatitis via suppressing acinar cell ferroptosis. *Br. J. Pharm.* **181**, 4067–4084 (2024).
45. Gu, X. et al. Ferroptosis exacerbates hyperlipidemic acute pancreatitis by enhancing lipid peroxidation and modulating the immune microenvironment. *Cell Death Discov.* **10**, 242 (2024).
46. Sindhu, S. et al. Neutral sphingomyelinase-2 and cardiometabolic diseases. *Obes. Rev.* **22**, e13248 (2021).
47. Green, C. D., Maceyka, M., Cowart, L. A. & Spiegel, S. Sphingolipids in metabolic disease: The good, the bad, and the unknown. *Cell Metab.* **33**, 1293–1306 (2021).
48. Manzo, O. L. et al. Rewiring endothelial sphingolipid metabolism to favor S1P over ceramide protects from coronary atherosclerosis. *Circ. Res.* **134**, 990–1005 (2024).
49. Ma, C. J. et al. Theasaponin E1 induce ferroptotic cell death in pomacea canaliculata through coordinated disruption of cholesterol homeostasis and sphingolipid metabolism. *J. Agric. Food Chem.* **73**, 29581–29592 (2025).
50. Chen, H. et al. Overcoming ELDR-mediated cancer cell survival in vitro and in vivo via sphingomyelin-driven TRPML1 inactivation and TFEB suppression through lysosomal HSP70 targeting. *Pharm. Res.* **222**, 108050 (2025).
51. Wang, R., Gao, C., Fan, Z., Qin, Q. & Zhan, H. Mitochondria-centric lipid metabolism and inter-organelle crosstalk in pancreatic Cancer: Unveiling novel therapies. *Cancer Lett.* **632**, 217965 (2025).
52. Yan, H. et al. Disturbing cholesterol/sphingolipid metabolism by squalene epoxidase arises crizotinib hepatotoxicity. *Adv. Sci.* **12**, e2414923 (2025).
53. Kim, G. T. et al. Upregulation of the serine palmitoyltransferase subunit SPTLC2 by endoplasmic reticulum stress inhibits the hepatic insulin response. *Exp. Mol. Med.* **54**, 573–584 (2022).
54. Xiao, J., Zeng, W., Zhang, P., Zhou, Y. & Fang, Q. Acid ceramidase targeting pyruvate kinase affected trypsinogen activation in acute pancreatitis. *Mol. Med.* **28**, 106 (2022).
55. Hagn-Meincke, R. et al. Circulating immune signatures in chronic pancreatitis with and without preceding acute pancreatitis: a pilot study. *Pancreatology* **24**, 384–393 (2024).
56. Nicholson, R. J., Norris, M. K., Poss, A. M., Holland, W. L. & Summers, S. A. The lard works in mysterious ways: ceramides in nutrition-linked chronic disease. *Annu. Rev. Nutr.* **42**, 115–144 (2022).
57. Olona, A. et al. Sphingolipid metabolism during Toll-like receptor 4 (TLR4)-mediated macrophage activation. *Br. J. Pharm.* **178**, 4575–4587 (2021).
58. Zheng, X. et al. Chaihu shugan powder ameliorated chronic pancreatitis by reprogramming SMS2-mediated sphingolipid metabolism in M1 macrophages. *Phytomedicine* **149**, 157565 (2025).
59. Wei, B. et al. Inhibition of TRAF6 improves hyperlipidemic acute pancreatitis by alleviating pyroptosis in vitro and in vivo rat models. *Biol. Direct* **18**, 23 (2023).
60. Qiao, O. et al. Rosmarinic acid plus deferasirox inhibits ferroptosis to alleviate crush syndrome-related AKI via Nrf2/Keap1 pathway. *Phytomedicine* **129**, 155700 (2024).
61. Ma, X. et al. Identification of AP-1 as a critical regulator of glutathione peroxidase 4 (GPX4) transcriptional suppression and acinar cell ferroptosis in acute pancreatitis. *Antioxidants* **12**, 100 (2022).
62. Zeng, Z. et al. Ferroptosis-related protein biomarkers for diagnosis, differential diagnosis, and short-term mortality in patients with sepsis in the intensive care unit. *Front. Immunol.* **16**, 1528986 (2025).
63. Fan, R., Sui, J., Dong, X., Jing, B. & Gao, Z. Wedelolactone alleviates acute pancreatitis and associated lung injury via GPX4 mediated suppression of pyroptosis and ferroptosis. *Free Radic. Biol. Med.* **173**, 29–40 (2021).
64. Al Mamun, A. et al. Pyroptosis in acute pancreatitis and its therapeutic regulation. *Apoptosis* **27**, 465–481 (2022).
65. Gao, L. et al. Acinar cell NLRP3 inflammasome and gasdermin D (GSDMD) activation mediates pyroptosis and systemic inflammation in acute pancreatitis. *Br. J. Pharm.* **178**, 3533–3552 (2021).
66. Jiang, J. et al. Hepatic sphingomyelin phosphodiesterase 3 promotes steatohepatitis by disrupting membrane sphingolipid metabolism. *Cell Metab.* **37**, 1119–1136.e13 (2025).
67. Wang, L. et al. A blood glucose fluctuation-responsive delivery system promotes bone regeneration and the repair function of Smpd3-reprogrammed BMSC-derived exosomes. *Int J. Oral. Sci.* **16**, 65 (2024).
68. Lecuyer, M., Pathipati, P., Faustino, J. & Vexler, Z. S. Neonatal stroke enhances interaction of microglia-derived extracellular vesicles with microglial cells. *Neurobiol. Dis.* **157**, 105431 (2021).
69. Sun, X., Yang, S., He, Z., Wang, L. & He, J. Integrated network pharmacology and transcriptomics to explore the mechanism of compound Dihuang granule (CDG) protects dopaminergic neurons by regulating the Nrf2/HMOX1 pathway in the 6-OHDA/MPP +-induced model of Parkinson's disease. *Chin. Med.* **19**, 170 (2024).

Acknowledgements

We thank Bullet Edits Limited for the linguistic editing and proofreading of the manuscript. This work was supported by the National Natural Science Foundation of China (Grant number: 82374248) and the Science and Technology Plan of Liaoning Province (Key Research and Development Program Project) (Grant number: 2025JH2/101800026).

Author contributions

Study Design and Amendments: A.H., Q.Y., J.C., Y.Y., S.C., L.W., D.S., P.Y. Coordinator for Multicenter Consultation and Communication: Y.Y., D.S., P.Y. Sample Collection: A.H., Q.Y., J.C., L.W., Y.Y., S.M., Z.W., S.C. Clinical and Metabolomics Data Collection: A.H., Q.Y., J.C., L.W., Y.Y., S.M., Z.W., S.C., P.Y. Data Analysis and Guidance: A.H., Q.Y., J.C., L.W., Y.Z., K.L., S.C., T.L., D.S., P.Y. Manuscript Writing: A.H., Q.Y., J.C., L.W. Manuscript Revising: S.C., T.L., D.S., P.Y. All authors finally approved publication of the manuscript.

Competing interests

Z.W. is co-founder of iPhenome Biotechnology Inc. Dalian (Yun Pu Kang). Other authors have declared that no competing interests exist.

Additional information

Supplementary information The online version contains supplementary material available at https://doi.org/10.1038/s41746-026-02792-2.

Correspondence and requests for materials should be addressed to Shengji Cao, Tianyi Liu, Dong Shang or Peiyuan Yin.

Reprints and permissions information is available at http://www.nature.com/reprints

Publisher's note Springer Nature remains neutral with regard to jurisdictional claims in published maps and institutional affiliations.

Open Access This article is licensed under a Creative Commons Attribution-NonCommercial-NoDerivatives 4.0 International License, which permits any non-commercial use, sharing, distribution and reproduction in any medium or format, as long as you give appropriate credit to the original author(s) and the source, provide a link to the Creative Commons licence, and indicate if you modified the licensed material. You do not have permission under this licence to share adapted material derived from this article or parts of it. The images or other third party material in this article are included in the article's Creative Commons licence, unless indicated otherwise in a credit line to the material. If material is not included in the article's Creative Commons licence and your intended use is not permitted by statutory regulation or exceeds the permitted use, you will need to obtain permission directly from the copyright holder. To view a copy of this licence, visit http://creativecommons.org/licenses/by-nc-nd/4.0/.

© The Author(s) 2026